Miscible, Porous Media Displacements with Density Stratification

AMIR RIAZ AND ECKART MEIBURG

Department of Mechanical and Environmental Engineering, University of California, Santa Barbara, California, USA

ABSTRACT: High accuracy, three-dimensional numerical simulations of miscible displacements with gravity override, in both homogeneous and heterogeneous porous media, are discussed for the quarter five-spot configuration. The influence of viscous and gravitational effects on the overall displacement dynamics is described in terms of the vorticity variable. Density differences influence the flow primarily by establishing a narrow gravity layer, in which the effective Péclet number is enhanced due to the higher flow rate. Although this effect plays a dominant role in homogeneous flows, it is suppressed to some extent in heterogeneous displacements. This is a result of coupling between the viscous and permeability vorticity fields. When the viscous wavelength is much larger than the permeability wavelength, gravity override becomes more effective because coupling between the viscous and permeability vorticity fields is less pronounced. Buoyancy forces of a certain magnitude can lead to a pinch-off of the gravity layer, thereby slowing it down.

KEYWORDS: miscible, porous media displacements; density stratification

INTRODUCTION

The stability of interfaces separating fluids of different viscosities in porous media has been the subject of numerous investigations since the pioneering work,[1–3] established that an adverse mobility ratio, that is, a less viscous fluid displacing a more viscous one, generates an unstable interface. By means of experiments and, more recently, numerical simulations, the nonlinear interfacial dynamics has been studied as well, using a variety of physical models and geometries, compare the review in Reference 4.

Accurate representation of the diffused interface in miscible displacements requires a high accuracy numerical method. A combination of spectral methods and high order, compact finite differences are employed to obtain very high accuracy in simulations of both two-dimensional rectilinear,[5,6] and quarter five-spot displacements.[7–9] The present investigation extends this approach to three dimensions, in order to analyze the interaction of viscous and gravitational effects in the quarter five-spot configuration.

Address for correspondence: Eckart Meiburg, Department of Mechanical and Environmental Engineering, University of California, Santa Barbara, CA 93106, USA. Voice/fax: 805-893-5278.
meiburg@engineering.ucsb.edu

Ann. N.Y. Acad. Sci. **1027: 342–359 (2004).** **©2004 New York Academy of Sciences.**
doi: 10.1196/annals.1324.029

The paper is organized as follows. The next section presents the governing equations and the boundary and initial conditions. Numerical implementation is discussed next. We then compare neutrally buoyant, two- and three-dimensional homogeneous displacements. The subsequent section presents the results of a parametric study, in which the effects of variation of density difference between the two fluids are investigated from a vorticity-based point of view for homogeneous displacements. The influence of heterogeneous permeability is then described. Finally, the last section highlights the main findings of this investigation and summarizes its most important conclusions.

GOVERNING EQUATIONS

The quarter five-spot arrangement consists of a staggered, doubly periodic array of injection and production wells, as shown in FIGURE 1. The mathematical model, described in detail elsewhere,[10] is based upon the vorticity formulation of Darcy's equation. We assume incompressible flow and use a convection–diffusion equation to advance the concentration field of the injected fluid. The computational domain is shown in FIGURE 2. To derive the dimensionless equations, we choose the side length L of the domain as the characteristic length scale. By denoting the source strength per unit depth as $2\pi Q$, we obtain the time and velocity scales as L^2/Q and Q/L, respectively. The viscosity μ_1 of the injected fluid is taken as the reference value for scaling the viscosities, whereas the difference between the fluid densities $\rho_2 - \rho_1$ provides a characteristic density value. Here the index 1 refers to the injected fluid and 2 denotes the displaced fluid. We define an aspect ratio $A = H/L$, where H is the domain height. The resulting governing equations in nondimensional form are

$$\nabla \cdot \mathbf{u} = 0, \tag{1}$$

$$\omega = \frac{1}{k}\nabla k \times \mathbf{u} + R\nabla c \times \mathbf{u} + \frac{Gk}{\mu}\nabla c \times \nabla z, \tag{2}$$

$$\frac{\partial c}{\partial t} + \mathbf{u} \cdot \nabla c = \frac{1}{Pe}\nabla^2 c. \tag{3}$$

For simplicity, we refer to the terms on the right hand side of the vorticity equation as *permeability vorticity, viscous vorticity,* and *gravitational vorticity.* Three dimensionless parameters appear in these equations

$$Pe = \frac{Q}{D}, \tag{4}$$

$$G = \frac{g(\rho_2 - \rho_1)KL}{Q\mu_1}, \tag{5}$$

$$R = -\frac{1}{\mu}\frac{d\mu}{dc} = \ln\left(\frac{\mu_2}{\mu_1}\right), \tag{6}$$

where c denotes the concentration of the injected fluid, k represents the isotropic permeability, and μ and ρ are the concentration dependent viscosity and density, respectively. We take the scalar diffusion coefficient to be a constant D. The dimensionless

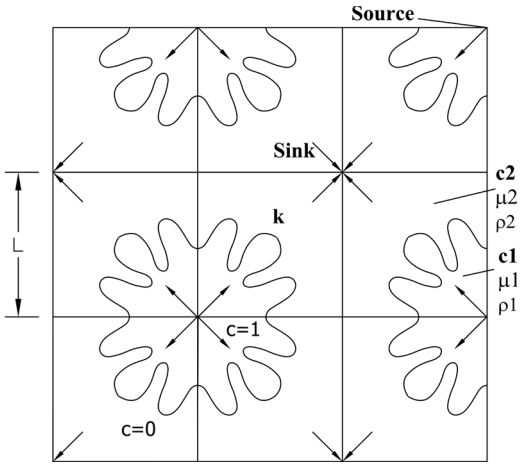

FIGURE 1. The quarter five-spot arrangement of injection and production wells.

parameters are the Péclet number *Pe*, the gravity parameter *G*, and the viscosity ratio parameter *R*.

The velocity is obtained through a three-dimensional vector potential[11] as

$$\mathbf{u} = \nabla \times \psi \tag{7}$$

$$\nabla^2 \psi = -\omega \tag{8}$$

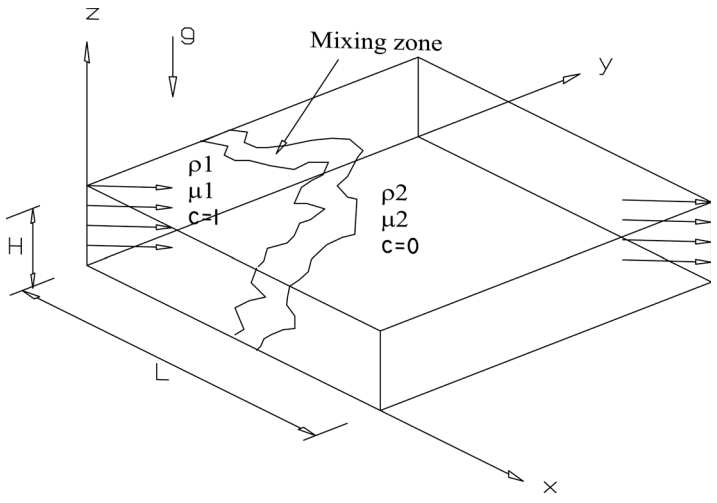

FIGURE 2. The three-dimensional computational domain.

At the vertical boundaries symmetry conditions are assumed. The top and bottom represent no-flux boundaries. By denoting the spatial components of ψ and ω as (ϕ, θ, χ) and (ξ, η, ζ), respectively, we obtain

$$x = 0, 1: \begin{cases} c_x = 0 \;\; k_x = 0 \\ u = 0 \quad v_x = 0 \;\; w_x = 0 \\ \phi_x = 0 \;\; \theta = 0 \quad \chi = 0 \\ \xi_x = 0 \;\; \eta = 0 \quad \zeta = 0 \end{cases} \tag{9}$$

$$y = 0, 1: \begin{cases} c_y = 0 \;\; k_y = 0 \\ u_y = 0 \;\; v = 0 \quad w_y = 0 \\ \phi = 0 \quad \theta_y = 0 \;\; \chi = 0 \\ \xi = 0 \quad \eta_y = 0 \;\; \zeta = 0 \end{cases} \tag{10}$$

$$z = 0, A: \begin{cases} c_z = 0 \;\; k_z = 0 \;\; w = 0 \\ \phi = 0 \quad \theta = 0 \quad \chi_z = 0 \end{cases} \tag{11}$$

To avoid an initially singular concentration distribution, we specify as the initial condition, at a small but finite time, the self-similar concentration profile corresponding to the radially symmetric problem.[12] It has the form

$$c_0 = \frac{1}{2}\left[1 + \mathrm{erf}\left(\sqrt{Pe}\left(\frac{r}{r_0} - 1\right)\right)\right], \tag{12}$$

where r_0 represents the initial radial location of the front. It determines the *effective starting time* $t_0 > 0$ of the computation as

$$t_0 = 0.5 r_0^2. \tag{13}$$

NUMERICAL IMPLEMENTATION

The numerical solutions are obtained with a combination of sixth-order compact finite difference[13] and spectral methods,[14,15] in conjunction with an explicit third-order time stepping scheme.

Time Stepping Scheme

The concentration field is advanced in time by an explicit third order Runga–Kutta method.[16] Writing the concentration Equation **(3)** as

$$\frac{\partial c}{\partial t} = F(c), \tag{14}$$

we obtain

$$c^k_{i,j} = c^{k-1}_{i,j} + \Delta t[\alpha_k F(c^{k-1}_{i,j}) + \beta_k F(c^{k-2}_{i,j})], \quad \textbf{(15)}$$

where

$$\alpha_1 = \frac{8}{15},\ \beta_1 = 0$$
$$\alpha_2 = \frac{5}{12},\ \beta_2 = -\frac{17}{60}$$
$$\alpha_3 = \frac{3}{4},\quad \beta_3 = -\frac{5}{12}.$$

Solution of the Poisson Equation

The solution procedure for the Poisson equation governing the vector potential is described for the example of the first component of Equation **(8)**

$$\phi_{xx} + \phi_{yy} + \phi_{zz} = -\xi. \quad \textbf{(16)}$$

Due to the periodicity in the x- and y-directions, this equation can be solved by a Fourier Galerkin method. The Fourier coefficients a_{ij} and b_{ij} of the vector potential and vorticity fields, respectively, are given by

$$\phi = \sum_{j=1}^{n-1}\sum_{i=1}^{n-1} a_{ij}(z)\cos[(i-1)\pi x]\sin[(j-1)\pi y] \quad \textbf{(17)}$$

$$\xi = \sum_{j=1}^{n-1}\sum_{i=1}^{n-1} b_{ij}(z)\cos[(i-1)\pi x]\sin[(j-1)\pi y]. \quad \textbf{(18)}$$

A second order ODE for $a_{ij}(z)$ is obtained by substituting Equations **(17)** and **(18)** into **(16)**

$$[-(i-1)^2\pi^2 - (j-1)^2\pi^2]a_{ij}(z) + a''_{ij}(z) = -b_{ij}(z). \quad \textbf{(19)}$$

By using compact finite differences to approximate d^2a/dz^2, we obtain the following pentadiagonal system

$$\alpha(a_{i,j,k-2} + a_{i,j,k+2}) + \beta(a_{i,j,k-1} + a_{i,j,k+1}) + \gamma a_{i,j,k} = -\frac{2}{11}b_{i,j,k-1} - b_{i,j,k} - \frac{2}{11}b_{i,j,k+1},$$

where

$$\alpha = \frac{3}{44\Delta^2}$$
$$\beta = -\frac{2}{11}[(i-1)^2 + (j-1)^2]\pi^2 + \frac{12}{11\Delta^2}$$
$$\gamma = -[(i-1)^2 + (j-1)^2]\pi^2 - \frac{24}{11}\Delta^2 - \frac{3}{22\Delta^2}.$$

A fine spatial and temporal resolution is required in order to resolve accurately all the length scales present in the domain, especially at high Péclet numbers. Time steps as small as $O(10^{-6})$ are used, whereas typical spatial resolutions employ

256×256×32 modes; that is, 2×10^6 grid points. For some parameter values a spatial resolution of 513×513×64 are used. A preliminary analysis was conducted to determine the appropriate grid spacing for various parameter combinations. An important criterion in this regard is the cutoff mode provided by the linear stability analysis.[12,17] The grid spacing is required always to be smaller than the cutoff wavelength. In addition, we also track the energy in the highest Fourier mode and require it to be less than 0.001% of the maximum energy in the spectrum. We also require the maximum and minimum numerical concentration levels to remain between 1.001 and –0.001, respectively, We have found that these particular values of the constraints guarantee convergence and stability of the numerical results. Our numerical algorithm is parallelized for optimal performance.[18]

COMPARISON BETWEEN TWO- AND THREE-DIMENSIONAL, NEUTRALLY BUOYANT DISPLACEMENTS

For a neutrally buoyant displacement without externally imposed initial perturbations in the vertical direction, the present three-dimensional algorithm exactly reproduces the two-dimensional results reported elsewhere.[7] In order to trigger a three-dimensionally evolving flow, we introduce random initial concentration perturbations of the form

$$c(x, y, z, t_0) = c_0(x, y, t_0) + \gamma f(x, y, z) e^{\frac{-(r-r_0)^2}{\sigma^2}}, \qquad \textbf{(20)}$$

where γ denotes the disturbance amplitude, f represents a field of random numbers uniformly distributed in the interval [−1, 1], and σ specifies the width of the initially perturbed layer around the mean interface position r_0. The simulations to be discussed below employ $\gamma = 0.025$ and $\sigma = 0.003$, as well as an initial interface location of $r_0 = 0.2$.

Random initial perturbations of the above form give rise to substantial fingering activity from the very start. FIGURE 3 presents a simulation for $Pe = 800$, $R = 2.5$, and $G = 0$; that is, without density contrast. The number of fingers in both the horizontal and vertical planes at early times are consistent with the linear stability results, as shown in FIGURE 3 A. The number of fingers is greatly reduced at later times, as seen

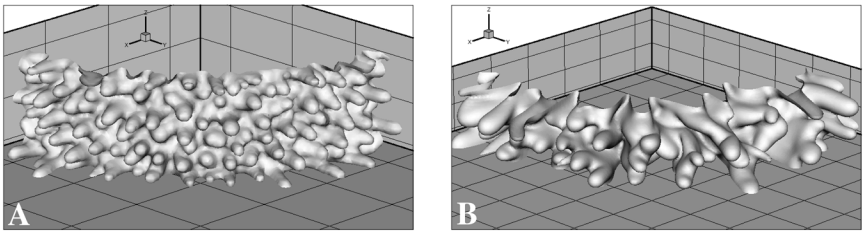

FIGURE 3. Concentration iso-surfaces obtained for random initial perturbations and $G = 0$, $Pe = 800$, $R = 2.5$, and $A = 1/8$, at times **(A)** 0.04 and **(B)** 0.14. Nonlinear interaction mechanisms of merging, shielding, and fading can be observed.

in FIGURE 3B. This is expected, both on the basis of linear stability results for vertical modes, as well as due to the nonlinear mechanisms of finger interaction, that is, merging and shielding.[5]

The magnitude of disturbances is obtained from the norm of vorticity, which is defined by

$$\|\omega(t)\| = \sqrt{\frac{1}{LNM}\sum_{i=1}^{L}\sum_{j=1}^{N}\sum_{k=i}^{M}\omega(t)^2_{i,j,k}}. \quad \textbf{(21)}$$

A quantitative comparison between the two- and three-dimensional displacements is given in FIGURE 4. The higher vorticity level in the three-dimensional simulation reflects a strong finger growth, which eventually leads to an earlier breakthrough, as shown in FIGURE 4. Here the breakthrough time t_b is defined as the time when the concentration of the injected fluid first reaches 1% somewhere along the height of the production well. Correspondingly, the overall efficiency η of the displacement process is given as the fraction of the total domain volume occupied by the injected fluid at the time of breakthrough, $\eta = \pi t_b/2$.

Comparison of the vorticity magnitudes in FIGURE 4 indicates a significant difference between two- and three-dimensional displacements in the quarter five-spot geometry, even for neutrally buoyant flows. This is somewhat unexpected in light of other findings,[19,20] where only small differences between two- and three-dimensional rectilinear flows were observed. This is attributed to the lack of a vortex stretching term in Darcy's flow,[19] since it is this term that causes quite fundamental differences

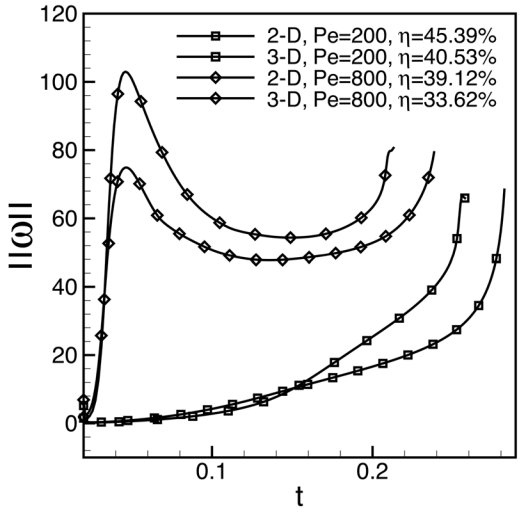

FIGURE 4. Comparison of the vorticity norm for the two- and three-dimensional cases for two different Péclet numbers. Higher vorticity values in the three-dimensional case result in a lower efficiency as compared to the two-dimensional case, for both small and large *Pe*. The higher vorticity level in the three-dimensional case results from the additional instability toward axial waves.[17]

between two- and three-dimensional flows governed by the Navier–Stokes equations. For quarter-spot displacements on the other hand, the higher vorticity level for three-dimensional displacements is due to an effective redistribution of the concentration gradient associated with the changes in the wavelength ratio of the most amplified vertical and horizontal waves.[17] Consequently, higher overall concentration fluctuations than in the purely two-dimensional case generate faster growing fingers for the three-dimensional case, which leads to an earlier breakthrough.

In order to demonstrate the validity of the simulations for the nonlinear stages, FIGURE 5 compares the present two- and three-dimensional simulation data for the displacement efficiency with experimental results.[21,22] The experiments quoted do not provide sufficient information to calculate a Péclet number. However, numerical simulations performed at $Pe = 800$ agree reasonably well with the experimental data for various viscosity ratios. The three-dimensional simulations are seen to lead to better agreement than their two-dimensional counterparts, especially at high viscosity ratios. Different Pe values result in somewhat different values of η, however, the trend of a continued decrease in η with R at large R values is more accurately represented by the three-dimensional simulations, independent of Pe. Similarly, the inclusion of a dispersion model would be expected to result in somewhat different values of η.

Three-dimensional simulations more accurately represent the displacement process by accounting for interaction between the horizontal and the vertical modes. We quantify this interaction by analyzing the relative magnitude of the norm for the vertical and the horizontal components of viscous vorticity. FIGURE 6 shows that the

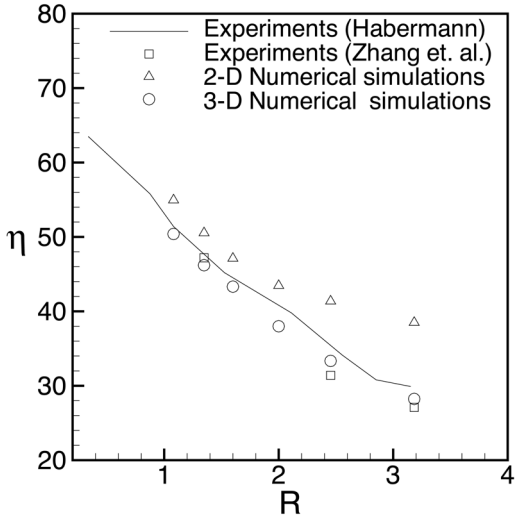

FIGURE 5. Displacement efficiency as a function of the viscosity ratio. Experimental data[21,22] are compared with numerical two-dimensional data for $Pe = 800$ (obtained with the present three-dimensional code using two-dimensional initial perturbations), and with the present three-dimensional data for $Pe = 800$. The three-dimensional results exhibit significantly better agreement with the experimental data.

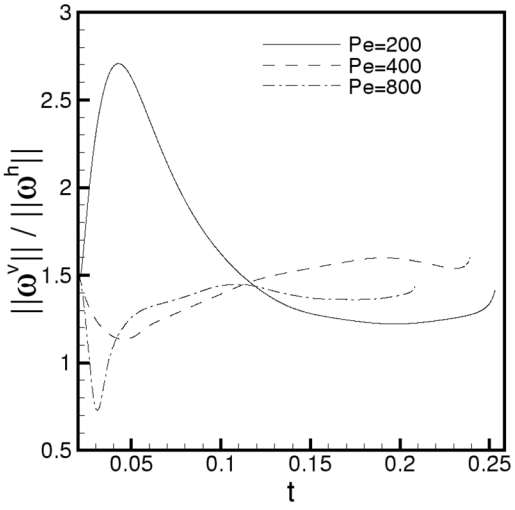

FIGURE 6. Ratio of the vertical to the horizontal vorticity norm for various values of Pe, $R = 2.5$, $G = 0$, and $A = 1/8$. $\|\omega^v\| / \|\omega^h\|$ gives the relative strength of the horizontal and the vertical disturbances, respectively. For initial time $t < 0.05$, horizontal modes dominate for $Pe = 200$ whereas vertical modes gain in strength for $Pe = 400$ and 800. A minimum value of the ratio is observed for $t > 0.12$ as a function of Pe.

horizontal modes, associated with vertical vorticity, dominate early on at time $t < 0.05$ for both $Pe = 200$ and 400, when $\|\omega^v\| / \|\omega^h\| > 1$. However, the negative slope of $\|\omega^v\| / \|\omega^h\|$ for $Pe = 400$ and early times shows that the energy in the vertical modes is growing at a higher rate. For $Pe = 800$, the ratio soon drops below 1, indicating the dominance of the vertical modes. This relative importance of the vertical modes at early times, for $Pe = 400$ and 800, is predicted by linear stability theory.[17] The situation subsequently changes due to the onset of nonlinear behavior. It is important to note that for later times $\|\omega^v\| / \|\omega^h\| > 1$, which indicates that the horizontal modes play a relatively more important part in the displacement dynamics. Also note that at later times $\|\omega^v\| / \|\omega^h\|$ exhibits a minimum. This reflects the fact that for large Pe values the strength of the vertical vorticity is reduced as a result of nonlinear interactions among the horizontal modes. The dominance of the horizontal modes is due to the mean flow in the horizontal planes. Additional simulations show that $\|\omega^v\| / \|\omega^h\|$ is independent of the aspect ratio, but only for neutrally buoyant displacements. Interaction between the horizontal and vertical modes qualitatively changes in displacements with gravity override, as is discussed below.

HOMOGENEOUS DISPLACEMENTS WITH GRAVITY OVERRIDE

In the following, we discuss the influence of the governing dimensionless parameter G on the overall features of the displacement process in a homogeneously permeable domain. How those flows are altered by the effects of density stratification

in comparison with the purely viscous instability studied by Chen and Meiburg[7] will be one of the main issues to be analyzed here.

FIGURE 7 presents concentration contours for the case of $Pe = 800$, $R = 2.5$, $G = 0.5$, and $A = 1.8$; that is, all parameters except G have the same values as in FIGURE 3. The simulation employs a grid of size $257 \times 257 \times 32$, as well as a time step of $O(10^{-6})$. The injected fluid, being lighter than the displaced fluid, tends to rise towards the upper boundary of the domain. A *gravity layer* is thus established in which the flow rate is higher than elsewhere in the domain. Both the gravity layer as well as the *underride* region below it give rise to well developed fingers as early as $t = 0.04$. The number of fingers decreases as the interface evolves due to both horizontal and vertical interactions among the fingers (cf., FIG. 7B). The thickness of the gravity layer is seen to increase, due to multiple mergers with the fingers directly below it. It is important to note the wide range of length scales produced during the displacement.

At $t = 0.14$ the growth of the fingers along the diagonal in the gravity layer is temporarily slowed by fingers approaching from below (FIG. 7C). The resulting buoyancy induced pinch-off effect,[6] cuts off the fluid supply of high velocity fingers in the gravity layer and leads to their gradual fading. This gives a chance to fingers farther away from the diagonal to break through first at $t = 0.21$. The pinch-off mechanism thus delays the time of breakthrough.

Closely related to the structure of the interface is the vorticity field. Equation **(2)** shows that vorticity is generated due to concentration gradients, which in turn determine the velocity field. Equation **(2)** also shows that gravitational vorticity compo-

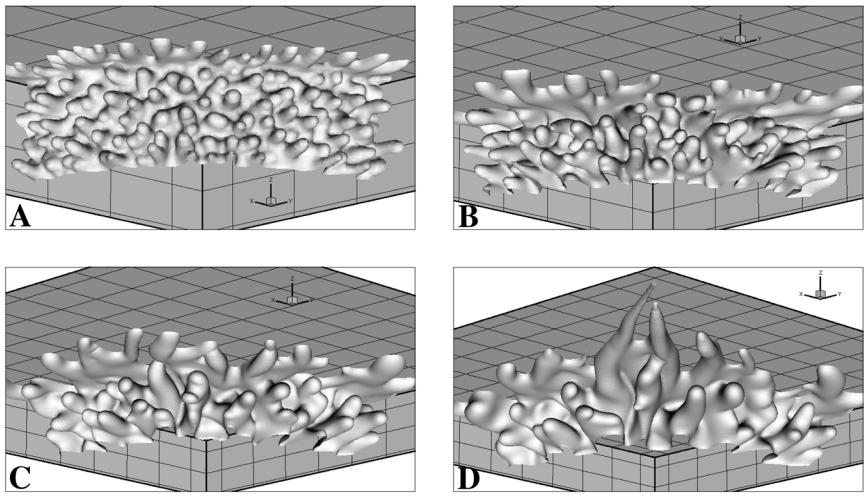

FIGURE 7. Concentration iso-surfaces for $Pe = 800$, $R = 2.5$, $G = 0.5$, and $A = 1/8$ at times 0.04, 0.08, 0.14, and 0.21. A gravity layer with numerous fingers evolves early on and becomes dominant around $t = 0.14$. The coupling of viscous and gravitational instability renders the gravity layer susceptible to a pinch-off by the underride fingers. Breakthrough is achieved by fingers in the gravity layer at $t = 0.21$.

nents can reinforce or cancel directly only the horizontal viscous vorticity components. FIGURE 8 plots isosurfaces of the viscous and gravitational vorticity components for the flow shown in FIGURE 7. Dark (light) shading represents negative (positive) values of vorticity. The horizontal and vertical components of the viscous vorticity are seen to form elongated dipole structures along the edges of the fingers, whereas the gravitational vorticity develops a more complex spatial structure. The buoyancy driven pinch-off shown in FIGURE 7B and C occurs due to the local reinforcement of the horizontal components of viscous and gravitational vorticity. Note that the spatial distribution of the gravitational vorticity shown in the figure is similar, but of opposite sign to that of the vertical viscous vorticity. This reflects the fact that both the vertical viscous vorticity and the gravitational vorticity are associated with horizontal concentration gradients.

We now consider a situation with a larger density contrast. FIGURE 9 depicts concentration isosurfaces from a simulation with the same parameter values as above, except that $G = 2$. The mesh size here is $513 \times 513 \times 64$. A strong gravity layer develops, in which the effective local Péclet number is large enough to sustain multiple tip splitting events. Most importantly, the gravity layer becomes increasingly dominant and moves far ahead of the underride region. The fingering activity in the underride region is subdued, as can be seen from a comparison of FIGURES 7C and 9B. Hence we note that increasing G values stabilize the underride region. This form of shear stabilization is studied in detail elsewhere.[23] In the present case, it has a detrimental effect on the overall efficiency of the displacement process, because it

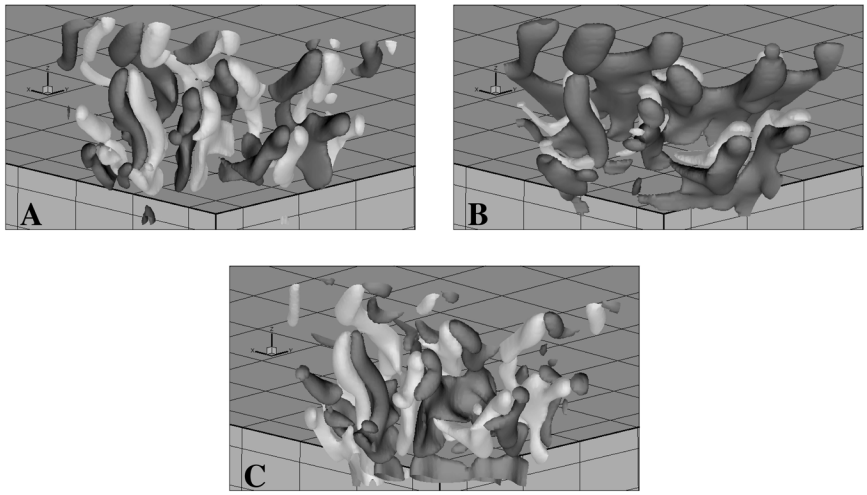

FIGURE 8. Iso-surfaces of **(A)** vertical viscous, **(B)** horizontal viscous, and **(C)** gravitational vorticity components for $Pe = 800$, $R = 2.5$, $G = 0.5$, and $A = 1/8$ at $t = 0.14$. The buoyancy driven interaction occurs due to the local reinforcement of the horizontal components of viscous and gravitational vorticity. The spatial distribution of gravitational vorticity is similar in shape, but of opposite sign to that of the vertical viscous vorticity.

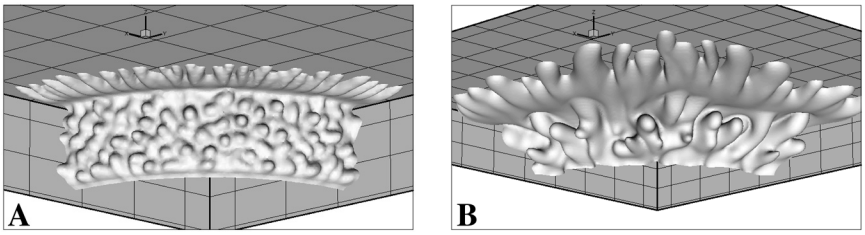

FIGURE 9. Concentration iso-surfaces for $G = 2.0$, $Pe = 800$, $R = 2.5$, and $A = 1/8$ at times **(A)** $t = 0.04$ and **(B)** $t = 0.14$. The gravity layer dominates the displacement. A significant reduction of the fingering activity in the underride region can be observed at this value of G. The breakthrough time is 0.165.

prevents the slowing of the gravity layer by pinch-off events. Consequently, the breakthrough time is reduced by almost 20% as G is increased from 0.5 to 2.

The influence of the gravity override mechanism can be evaluated by considering the relative strengths of waves in the horizontal and vertical directions, as reflected by the ratio of the vertical to the horizontal viscous vorticity in FIGURE 10. It is to be kept in mind that waves in a horizontal plane are associated with vertical vorticity and vice versa. FIGURE 10A shows the cases depicted in FIGURES 7 and 9, as well as a case for $G = 0.25$. The ratio $\|\omega^v\| / \|\omega^h\|$ decreases uniformly with an increase in G, reflecting the emergence of a strong gravity layer. Throughout the displacement process, the interplay of vertical and horizontal vorticity components is strongly affected by G. A comparison of the efficiencies listed in FIGURE 10A shows that the

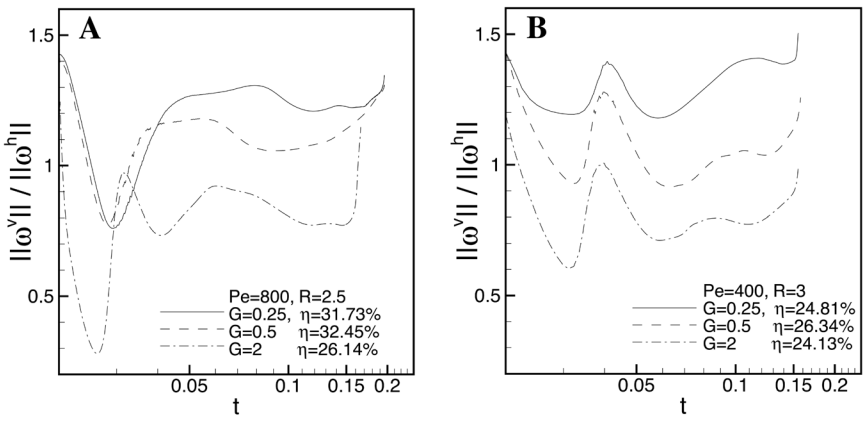

FIGURE 10. Ratio of the norms of vertical to horizontal viscous vorticity components as a function of G. Increase in G uniformly strengthens the vertical component of viscous vorticity. Optimal interaction between the horizontal and the vertical modes is given by $\|\omega^v\| / \|\omega^h\| \approx 1$.

maximum efficiency is achieved at $G = 0.5$, as an optimal interaction between the two components is achieved with the ratio $\|\omega^v\| / \|\omega^h\|$ close to unity throughout the displacement process. A similar optimal behavior is observed in FIGURE 10B for $G = 0.5$. A possible interpretation of the optimal interaction phenomenon is that the initial dominance of vertical viscous vorticity develops the underride fingers, and the later dominance of buoyancy effects allows these fingers to pinch off the gravity layer. If G is too large, the underride fingers do not develop to a point where a meaningful interaction with the gravity layer can be sustained. On the other hand, if G is too small, the gravity effect is not strong enough to allow the underride fingers to curve upward and pinch off the gravity layer. Note that the optimal interaction mechanism is very sensitive to the interfacial structure, which is in turn strongly dependent upon the initial conditions. Given the high cost of numerical simulations, we have not carried out a detailed study of this phenomenon. On the other hand, a gain of a few percent in efficiency can be important for enhanced oil recovery processes, so that a detailed investigation of this phenomenon would appear to be a worthwhile pursuit.

HETEROGENEOUS DISPLACEMENTS WITH GRAVITY OVERRIDE

Spatial permeability variation introduces an additional vorticity component related to permeability, as given by Equation **(2)**. Details about constructing a random permeability field k with horizontal and vertical wavelengths m and n, respectively, and variance s are given elsewhere.[24] From the previous section we see that if the injected fluid is lighter than the displaced fluid gravitational vorticity can give rise to a gravity layer that substantially alters the characteristics of the flow.[6,25] Within the gravity layer the fingers are enhanced, whereas in the underride region they are suppressed.

For homogeneous quarter five-spot displacements, a larger gravity parameter G generally results in earlier breakthrough, although for some parameter combinations intermediate values of G have been observed for which the efficiency is optimized due to specific interactions between the horizontal and vertical modes.[10] Two-dimensional rectilinear displacements[26] demonstrate that the effect of gravity override is considerably reduced by permeability heterogeneities, due to the coupling between the viscous and permeability vorticities. As a result, an optimal efficiency is achieved at an intermediate variance level.

The influence of gravity override is shown in FIGURE 11 for a representative combination of displacement parameters, at various values of the gravity parameter G. Comparison of the $G = 0.5$ case in FIGURE 11B with the $G = 0$ case in FIGURE 11A shows that gravity override strengthens the fingers close to the upper boundary, while weakening those near the lower boundary. Although the gravity layer is not as pronounced for the present, heterogeneous case as it is for the corresponding homogeneous case,[10] a slight diversion of the flow from the underride region to the gravity layer for $G = 0.5$ slows the rapid movement of the dominant fingers in the underride region observed for $G = 0$ in FIGURE 11A. Consequently, for the case $G = 0.5$, FIGURE 11B shows that the gravity layer fingers are slightly stronger as compared to the $G = 0$ case, which results in an improvement of the efficiency. It should be pointed out that the maximum in the recovery curve for an intermediate G in the

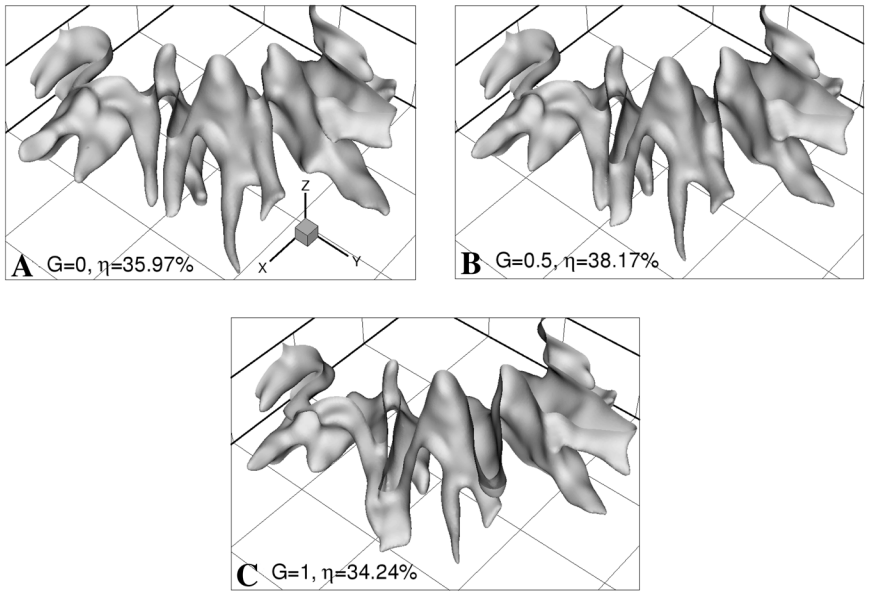

FIGURE 11. Concentration isosurfaces for the gravity override case. $Pe = 400$, $R = 2.5$, $s = 0.1$, $m = 20$, $n = 20$, $t = 0.14$ and various values of G. By encouraging the development of a gravity layer along the top boundary, the dominant fingers close to the lower boundary are weakened resulting in an improvement in efficiency as G goes from 0 to 0.5. Further increase in the gravity override effect at $G = 1$ strengthens the fingers in the gravity layer resulting in a reduction in efficiency. Due to the coupling between viscous and permeability vorticities, the gravity override effect is weaker than in homogeneous displacements.

above case is due to the location of the dominant flow path in the underride region. If the flow path with the lowest resistance were instead located close to the upper boundary, there would be a monotonic decrease in efficiency with increasing G.

Note that the gravity layer is relatively weak for the present, heterogeneous case, as compared to the corresponding homogeneous flow.[10] This fact, which is similar to observations for rectilinear flows, indicates that at the level of $s = 0.1$ the heterogeneity is already too strong for the coupling between the viscous and permeability vorticities to be effectively modified by the gravitational vorticity component. This is confirmed by FIGURE 12, which depicts the same flows as FIGURE 11, except that $s = 0.01$. Here the gravity layer is much stronger, which leads to a lower breakthrough efficiency for $s = 0.01$ than for $s = 0.1$, for both $G = 0.5$ and 1.

The above observation reflects the fact that the dominant path is selected not only on the basis of its permeability. Also important is its potential to support a resonant amplification, which partly depends on its geometric nature, and also on the local flow rate, which in turn is a function of the overall gravitational effect. Hence, the flow can select a relatively low permeability path over one with higher permeability, as long as it supports a strong resonant amplification.

The relatively weak dependence of heterogeneous displacements on the gravity parameter, as compared to their homogeneous counterparts, is also reflected in the norms of the vertical and horizontal viscous vorticity fields. Since gravitational effects primarily result in horizontal vorticity, it is instructive to analyze the ratio of the vertical to the horizontal viscous vorticity norms $\|\omega_v^v\| / \|\omega_v^h\|$, shown in FIGURE 13. We vary both the horizontal (*m*, FIG. 13A) and the vertical (*n*, FIG. 13B) permeability wave number. In each case the homogeneous displacement is more strongly affected by the horizontal vorticity (i.e., by gravitational effects) than any of the heterogeneous displacements. Note that the influence of gravity, $\|\omega_v^v\| / \|\omega_v^h\|$ decreases with *m* and it increases with *n*.

Individual random realizations of the permeability field can strongly influence the fingering dynamics, and consequently the displacement efficiency.[24] We have not attempted to run sufficiently many simulations in order to obtain statistically significant averages, due to the prohibitive computational expense. Instead, we have limited ourselves to identifying the generic mechanisms that govern heterogeneous displacements. The accurate prediction of the displacement efficiency for a specific permeability field would, of course, require complete knowledge of the permeability distribution.[27]

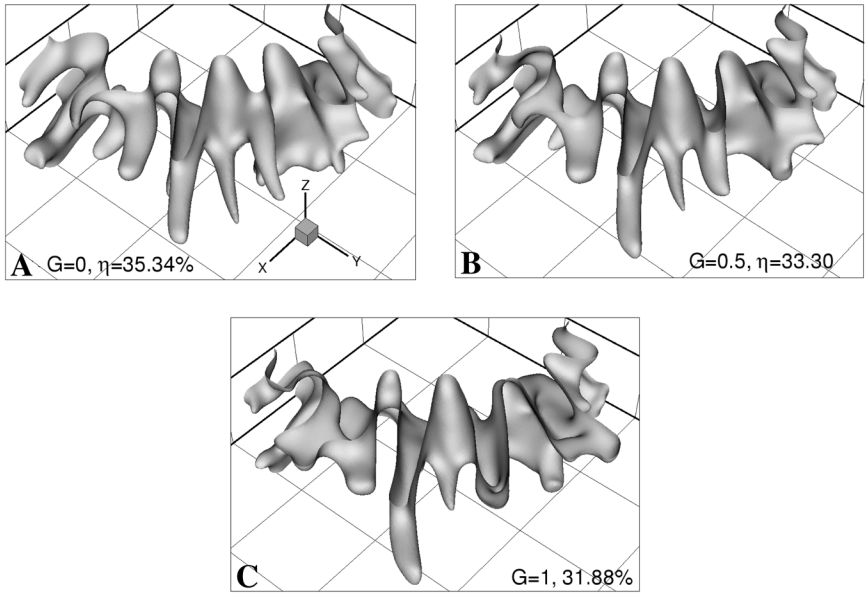

FIGURE 12. Concentration isosurfaces for the same cases as in FIGURE 11, but with a lower variance, $s = 0.01$. The lower level of heterogeneity allows the gravity layer to develop relatively freely, which results in a monotonic decrease in efficiency. The higher efficiency for $s = 0.1$ as compared to $s = 0.01$ for $G = 0$ is due to a weakening of the gravity layer, as well as the strengthening of the off-diagonal fingers, at $s = 0.1$.

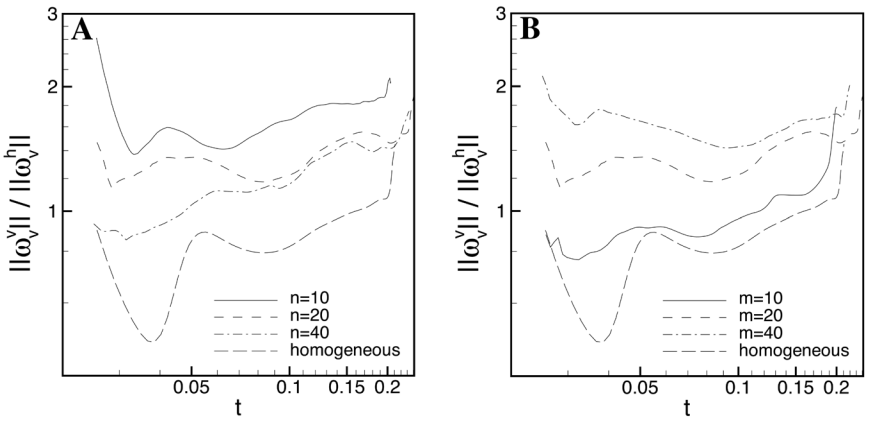

FIGURE 13. Ratio of the vertical and horizontal viscous vorticity norm. $Pe = 400$, $R = 2.5$, $G = 0.5$, $s = 0.1$, $A = 1.8$, **(A)** $n = 20$, **(B)** $m = 20$. Gravity override increases the relative strength of disturbances in the vertical direction, which are associated with horizontal vorticity. For the homogeneous case $\left\|\omega_v^v\right\| / \left\|\omega_v^h\right\| < 1$. On the other hand, the ratio exceeds unity for most heterogeneous cases, which implies that the perturbations in the horizontal directions are dominant. The ratio decreases with increasing m and it increases with n.

CONCLUSIONS

The present investigation employs high accuracy numerical simulations in order to analyze three-dimensional miscible displacements with gravity override in the quarter five-spot geometry. Even for neutrally buoyant displacements, three-dimensional effects are seen to change the character of the flow in a way that cannot be anticipated from two-dimensional simulations alone. This is in contrast to the case of rectilinear miscible flows, for which the inclusion of the third dimension is found[19,25] to have generally small effects. Part of the difference between two- and three-dimensional quarter five-spot flows can be attributed to the enhanced interaction of disturbances in three dimensions, resulting from the time dependence of the most amplified axial mode.[17] By forcing a large scale redistribution of concentration gradients, the temporal change of the axial wave number introduces an additional source of instability in the system.

Density differences have a significant influence on the displacement, primarily through the production of a narrow gravity layer that bypasses much of the resident fluid to arrive at the production side ahead of the underride region, thereby reducing the displacement efficiency. However, for certain parameter combinations buoyancy forces of the right magnitude can pinch off the gravity layer and hinder its movement towards the production well.

The interaction of viscous and gravitational effects is analyzed on the basis of their respective contributions to the temporal evolution of the vorticity field. The gravitational effect is associated with an increase in the horizontal vorticity component, whereas the viscous effect is related to both horizontal and vertical vorticity

components. As expected, the gravitational effect primarily operates on vertical disturbances.

In the presence of density differences, the potential for gravity override becomes important. Although this effect is seen to play a dominant role in homogeneous displacements, it is suppressed to some extent in heterogeneous displacements, even for relatively small values of the heterogeneity variance. This is a result of the coupling between viscous and permeability vorticity fields. For small vertical permeability wavelength relative to the viscous wavelength, gravity override is somewhat more effective because the coupling between viscous and permeability vorticity fields is less pronounced, so that the large scale fingering structures become more responsive to buoyancy effects. This is confirmed by the ratio of the vertical to the horizontal viscous vorticity norm, which decreases with increasing values of the vertical correlation wave number.

ACKNOWLEDGMENT

The authors thank Dr. Hamdi Tchelepi for several helpful discussions. Support for this research by the Petroleum Research Fund, the Department of Energy, Chevron Petroleum Technology Company, as well as through an NSF equipment grant and the San Diego Supercomputer Center is gratefully acknowledged.

REFERENCES

1. HILL, S. 1952. Channeling in packed columns. Chem. Engng. Sci. **1:** 247.
2. SAFFMAN, P.G. & G.I. TAYLOR. 1958. The penetration of a fluid into a porous medium or Hele-Shaw cell containing a more viscous liquid. Proc. R. Soc. London Ser. A **245:** 312.
3. CHOUKE, R.L., P.V. MEURS & C.V.D. POEL. 1959. The instability of slow, immiscible, viscous liquid-liquid displacements in permeable media. Trans. AIME **216:** 188.
4. HOMSY, G.M. 1987. Viscous fingering in porous media. Annu. Rev. Fluid Mech. **19:** 271.
5. TAN, C.T. & G.M. HOMSY. 1988. Simulation of nonlinear viscous fingering in miscible displacement. Phys. Fluids **31**(6): 1330.
6. RUITH, M. & E. MEIBURG. 2000. Miscible rectilinear displacements with gravity override. Part 1. Homogeneous porous medium. J. Fluid Mech. **420:** 225.
7. CHEN, C.-Y. & E. MEIBURG. 1998. Miscible porous media displacements in the quarter five-spot configuration. Part 1. The homogeneous case. J. Fluid Mech. **371:** 233.
8. CHEN, C.-Y. & E. MEIBURG. 1998. Miscible porous media displacements in the quarter five-spot configuration. Part 2. Effect of heterogeneities. J. Fluid Mech. **371:** 269.
9. CHEN, C.-Y. & E. MEIBURG. 2000. High-accuracy implicit finite-difference simulations of homogeneous and heterogeneous miscible porous medium flows. SPE J. **5**(2): 129.
10. RIAZ, A. & E. MEIBURG. 2003. Three-dimensional miscible displacement simulations in homogeneous porous media with gravity override. J. Fluid Mech. **494:** 95.
11. FLETCHER, C.A.J. 1991. Computational techniques for fluid dynamics, second ed., vol. 2 of Springer series in computational physics. Springer.
12. TAN, C.T. & G.M. HOMSY. 1987. Stability of miscible displacements in porous media: radial source flow. Phys. Fluids **30**(5): 1239.
13. LELE, S.K. 1992. Compact finite differences with spectral-like resolution. J. Comput. Phys. **103:** 16.
14. GOTTLIEB, D. & S.A. ORSZAG. 1977. Numerical Analysis of Spectral Methods: Theory and Applications. Society for Industrial and Applied and Mathematics.

15. CANUTO, C. M.Y. HUSSAINI, A. QUARTERONI & T.A. ZANG. 1986. Spectral Methods in Fluid Dynamics. Springer Series in Computational Dynamics. Springer-Verlag.
16. WRAY, A.A. 1991. Minimal storage time-advancement schemes for spectral methods. Preprint.
17. RIAZ, A. & E. MEIBURG. 2003. Radial source flows in porous media: linear stability analysis of axial and helical perturbations in miscible displacements. Phys. Fluids **15**(4): 938.
18. RIAZ, A. 2003. Three-Dimensional Miscible, Porous Media Displacements in the Quarter Five-Spot Geometry. PhD Thesis, Department of Mechanical and Environmental Engineering. University of California, Santa Barbara.
19. ZIMMERMAN, W.B. & G.M. HOMSY. 1992. Three-dimensional viscous fingering: a numerical study. Phys. Fluids **4**(9): 1901.
20. TCHELEPI, H.A. 1994. Viscous Fingering, Gravity Segregation and Permeability Heterogeneity in Two-Dimensional and Three-Dimensional Flows. PhD Thesis, Department of Petroleum Engineering, School of Earth Sciences, Stanford University.
21. HABERMANN, B. 1960. The efficiency of miscible displacement as function of mobility ratio. Trans. AIME **219:** 264.
22. ZHANG, H.R., K.S. SORBIE & N.B. TSIBUKLIS. 1997. Viscous fingering in five-spot experimental porous media: new experimental results and numerical simulations. Chem. Engng. Sci. **52:** 37.
23. ROGERSON, A. & E. MEIBURG. 1993. Shear stabilization of miscible displacements in porous media. Phys. Fluids **5**(6); 1344.
24. RIAZ, A. & E. MEIBURG. 2004. Vorticity interaction mechanisms in variable viscosity, heterogeneous miscible displacements with and without density contrast. J. Fluid Mech. To appear.
25. TCHELEPI, H.A. & F.M.J. ORR. 1994. Interaction of viscous fingering, permeability inhomogeneity and gravity segregation in three dimensions. SPE Res. Eng. **9**(4): 266.
26. CAMHI, E., M. RUITH & E. MEIBURG. 2000. Miscible rectilinear displacements with gravity override. Part 2. Heterogeneous porous media. J. Fluid Mech. **420:** 259.
27. ZHAN, L. & Y.C. YORTSOS. 2001. A direct method for the identification of the permeability field of an anisotropic porous medium. Water Resour. Res. **37**(7): 1929.